PAPER

Check for updates

Design and synthesis of MOF-derived CuO/g-C₃N₄ composites with octahedral structures as advanced anode materials for asymmetric supercapacitors with high energy and power densities†

Ziyang Zhu, Chuanying Wei, Di Jiang, Xinru Wu and Min Lu ⓘD *

In this study, two-component composites consisting of transition metal copper oxide (CuO) and graphite carbon nitride (g-C₃N₄) were successfully synthesized. Firstly, a typical metal–organic framework (MOF) material, namely CuBTC, was prepared by the hydrothermal method. Then, the hollow porous CuO/g-C₃N₄ composite with an octahedron structure was obtained by introducing a certain amount of g-C₃N₄ into the system using ultrasonic treatment and rapid thermal annealing. The synthesized CuO/g-C₃N₄ not only retains the unique octahedral morphology of the CuBTC template, but also is coated by a uniform carbon layer. This CuO/g-C₃N₄ displays a high reversible specific capacity (1530.4 F g⁻¹, 2 A g⁻¹) as an anode material. In addition, an asymmetric supercapacitor assembled with self-made NiCoMOF as the cathode and CuO/g-C₃N₄ as the anode achieves an excellent energy density of 50.8 W h kg⁻¹ at a power density of 800 W kg⁻¹ and stable cycling performance (70.1% capacity retention over 3000 cycles). These outstanding electrochemical properties are attributed to the synergistic effect between transition metal oxides and carbon-based materials as well as the unique structure of the composites, which also provides a facile design and synthesis idea to construct high-performance transition metal compounds with a unique hollow structure and C-coating for developing asymmetric supercapacitors with high energy and power densities.

1. Introduction

In recent years, with the development of wearable electronic devices and the innovation of energy technology, the demand for energy storage devices is more and more urgent.[1] Among them, supercapacitors have shown great development potential because of their fast charging and discharging speed, long cycle life and high power density.[2–6] However, in order to meet the increasing energy density requirements of the next generation of electronic devices, the energy density of ultracapacitors needs to be further improved. Compared with symmetric supercapacitors (SSCs), asymmetric supercapacitors (ASCs) exhibit excellent electrochemical performance due to their wider potential window which improves the energy density.[7–12] For the past few years, the development of cathode materials for hybrid capacitors has been rapid, while the development of anode materials is relatively slow. Carbon materials are widely used as anode materials in hybrid supercapacitors due to their

high specific surface area, excellent electrical conductivity and high power density.[13,14] However, the low specific capacitance (CSP) properties of carbon materials severely limit the energy density of ASCs. Therefore, seeking high-performance negative materials is still a hot and difficult topic in the future work.

Owing to the high theoretical specific volume, being rich in resources, inexpensiveness, and eco-friendliness, transition metal oxides (TMO) are widely used as electrode materials for supercapacitors (SCs).[15] In the anode materials, TMOs are getting more attention because of their high theoretical specific capacity, good chemical and thermal stability, easy synthesis, abundant resources and environment friendliness.[16–18] However, the volume expansion of TMOs is relatively serious during their repeated cycling, which leads to poor conductivity and cycling performance. Hence, it is feasible to effectively improve the electrochemical performance from two aspects of increasing the conductivity and inhibiting the volume expansion.[19,20]

At present, the introduction of carbon materials is the most commonly used electrode material strategy. Various types of carbon materials, for instance, zero-dimensional carbon quantum dots and carbon microspheres, one-dimensional carbon nanotubes and carbon nanofibers, two-dimensional graphene and

School of Chemical Engineering, Northeast Electric Power University, Jilin 132012, P. R. China

† Electronic supplementary information (ESI) available. See DOI: 10.1039/d1ma00766a

graphene oxide, three-dimensional graphene foam, *etc.*, have been successfully combined with transition metal oxides to construct excellent performance electrode materials.[21–28] Among them, graphite carbon nitride (g-C_3N_4) has appealed to more and more researchers, on account of its low cost, good chemical stability and mechanical stability.[29] The lone pair electrons of the N atom in g-C_3N_4 can strengthen the polarity of the molecule, which is beneficial to increase the transport efficiency of the charge carriers.[30] In addition, as a soft polymer, it is easy for g-C_3N_4 to compound with other materials, and its unique lamellar structure is conducive to the horizontal transfer of charges.[31–33] However, it is most critical for the direct introduction of an external carbon source to form a stable and firm interfacial bond between the active material and the carbon matrix.

In addition to optimizing the composition of the electrode material, it is significant to regulate the morphology and structure of the materials during the design process for their electrochemical performance.[34–36] It is well known that the hollow structure can improve the performance of the materials, due to their excellent physical and chemical properties such as lower-density, higher specific surface area, good penetrability and so on, which results in more active sites and more rapid capacity for charge transfer during redox reactions.[37–43] Moreover, the hollow structure can also alleviate volume expansion during charge and discharge, forming a great interface area between the electrode and electrolyte, which is convenient for charge transfer. Therefore, it is a major challenge to design and develop a kind of hollow porous electrode material with a special chemical composition and morphology. It is well known that as a self-sacrificing template, the metal organic frameworks (MOFs) can be used to synthesize active electrode materials with special morphologies because of their adjustable structure, variable composition and porosity.[44–46] For example, Guan *et al.* obtained NiCoO$_x$ materials with a multi-shell structure by rapid thermal oxidation using NiCoMOF as a precursor.[47] Xu *et al.* synthesized hollow spherical NiSe using NiBTC as a template.[48] Herein, we fabricated a hollow octahedral structured CuO/g-C_3N_4 composite with a uniform carbon coating by using the CuBTC as the precursor. By optimizing the heat treatment temperature and dosage of g-C_3N_4, the synthesized composite finally obtains unique advantages in structure and composition, and displays an excellent reversible specific capacity at a large current density (1530.4 F g^{-1}, 2 A g^{-1}) as an anode material. Subsequently, an ASC assembled with self-made NiCoMOF as the cathode and CuO/g-C_3N_4 as the anode achieves an excellent energy density of 50.8 W h kg^{-1} at a power density of 800 W kg^{-1} and stable cycling performance (70.1% capacity retention over 3000 cycles). Our strategy provides a facile design and synthesis idea to combine transition metal compounds with a special hollow structure and C-coating for exploitation of high-performance ASCs.

2. Experimental

2.1. Materials

p-Benzenedicarboxylic acid (PTA), Cu(NO$_3$)$_2$·6H$_2$O, 1,3,5-benzenetricarboxylic acid, Ni(NO$_3$)$_2$·6H2O, CoCl$_2$·6H$_2$O, melamine

and ammonium bicarbonate were purchased from Aladdin Reagents Company (China). *N*,*N*-Dimethylformamide and ethanol were purchased from Liaoning Quanrui Reagent Co., Ltd. All reagents were of analytical grade and no further purification was required. The deionized water in this work was used.

2.2. Preparation of precursors of CuBTC

CuBTC was prepared by a simple hydrothermal method without further purification. CuBTC was first dissolved in 1.932 g (8 mmol) Cu(NO$_3$)$_2$·6H$_2$O in 17 mL deionized water. Subsequently, 0.841 g (4 mmol) 1, 3, 5-benzenetricarboxylic acid was dissolved in the mixture of 17 mL DMF and 17 mL ethanol and stirred evenly. Then, the Cu(NO$_3$)$_2$ clarifying solution was laxly transferred into the homopolitriformic acid at a rate of 3 mL min^{-1}, and continued to be stirred for 6 h. All the mixtures were poured into a 100 mL Teflon-lined stainless steel reactor and reacted at 100 °C for 4 h. After natural cooling to room temperature, they were washed with DMF and anhydrous ethanol 3 times respectively. Finally, they were centrifuged and dried for 12 h under 60 °C vacuum conditions to get CuBTC.

2.3. Preparation of CuO/g-C_3N_4 composites

Using synthesized CuBTC as the template, the hollow porous CuO/g-C_3N_4 composites were prepared by ultrasonic composite incorporation and rapid annealing treatment. Firstly, g-C_3N_4 was prepared according to the reported method. After 1 g melamine powder and 0.3 g cyanamide carbonate powder were evenly mixed, the material was calcined at 600 °C for 4 h under a N$_2$ atmosphere at a heating rate of 5 °C min^{-1} to prepare g-C_3N_4. Then, the synthesized CuBTC and g-C_3N_4 were uniformly mixed at a mass ratio of 1 : 0.5 and treated with ultrasound for 30 min. Finally, the hollow porous CuO/g-C_3N_4 composite was obtained by rapid annealing of the mixed powder in air at 500 °C, and the annealing time is 10 min at the same heating rate. In contrast, all steps for the synthesis of pure CuO were similar except that g-C_3N_4 was not added. CuBTC was annealed directly to obtain pure CuO.

In order to obtain the best preparation method, the control variable method was used to adjust the experimental parameters. First of all, for the best conditions of CuO conversion, calcination time is determined to be 10 min, adjusting the calcination temperature range of 300–600 °C, labeled as CuO$_{300}$, CuO$_{400}$, CuO$_{500}$ and CuO$_{600}$. Through the electrochemical test, CuO$_{500}$ performance is the best. Then, in order to determine the best proportion of the compound, the mix proportion of g-C_3N_4 was adjusted at the best calcination temperature, which was 0.25, 0.5, 0.75, and 1.0, respectively. It is denoted as CuO/g-C_3N_4-0.25, CuO/g-C_3N_4-0.5, CuO/g-C_3N_4-0.75, and CuO/g-C_3N_4-1.0.

2.4. Materials characterization

The morphology and structure of the products were characterized by scanning electron microscopy (SEM; XL-30 FEG, FEI) and transmission electron microscopy (TEM; TECNAI F20, FEI). The as-prepared samples were tested by powder X-ray diffraction patterns, and observed with a Rigaku SmartLab Auto X-ray

diffractometer with Cu Kα radiation ($\lambda = 1.5418$ Å) in the range of 2–70. Thermogravimetric analysis (TGA) was adopted on an SDT Q600 (TA Instruments). The X-ray photoelectron spectroscopy (XPS) measurements were obtained with a Thermo Fisher Scientific EscaLab 250Xi XPS with monochromatic Al Kα radiation. The N2 adsorption–desorption isotherms were detected with a Micromeritics Tristar 3020 instrument in static mode, and specific surface area and pore structure were derived from the BET equation and Barrett–Joyner–Halenda (BJH) method.

2.5. Preparation and test of the electrode

The electrochemical properties of the as-synthesized samples were tested with a CHI 660E electrochemical workstation in 2 M KOH aqueous solution. All tests were performed in a traditional three-electrode system, consisting of a working electrode, a reference electrode (Hg/HgO electrode) and a counter electrode (platinum plate electrode). In detail, all of the working electrodes were made by the following steps: a certain amount of the active material, acetylene black and polytetrafluoroethylene (PTFE) emulsion were scattered in ethanol at a mass ratio of $8:1:1$ to come into being a uniform black slurry, which was subsequently coated on nickel foam (1.0 cm × 1.0 cm) under 10 MPa pressure for 30 s. In the end, the nickel foam with active substances was perched at 60 °C for 12 h. According to the galvanostatic charge–discharge results, the specific capacitance of the anodes was calculated on the basis of the following formula:

$$C = \frac{I \times \Delta t}{m \times \Delta V} \tag{1}$$

where C, I, Δt, m and ΔV are the specific capacitance (F g^{-1}), discharge current (A), discharge time (s), mass of the active material (g) and potential window (V), respectively.

2.6. Preparation of asymmetric supercapacitors

The first is the preparation of the cathode material. The NiCoMOF cathode material was obtained by the method reported in the literature.[49] The mass of 0.192 g Ni(NO$_3$)$_2$·6H$_2$O, 0.1178 g CoCl$_2$·6H$_2$O and 0.332 g (PTA) dispersed in 40 mL DMF, and the whole mixture for 1 h. Then, 4 mL 0.4 M sodium hydroxide is added drop by drop slowly to the above solution. The resulting mixture was converted into 100 mL Teflon-lined stainless steel autoclaves and maintained at a temperature of 100 °C for 8 h. After natural cooling, the precipitation was washed with DMF and anhydrous ethanol. Finally, the NiCoMOF cathode material was centrifuged and obtained by drying at 60 °C for 12 h.

Asymmetric supercapacitors were prepared using hollow porous CuO/g-C$_3$N$_4$ as the anode material, NiCoMOF as the cathode material, filter paper as the diaphragm and 6 M KOH as the electrolyte.

In addition, the energy density (E, W h kg^{-1}) and power density (P, W kg^{-1}) are two key indicators to assess the potential of supercapacitors in practical applications, which can be calculated by the following formulas:[50]

$$E = \frac{1}{2}C \times \Delta V^2 \tag{2}$$

$$P = \frac{E}{\Delta t} \tag{3}$$

where C (F g^{-1}), ΔV (V) and Δt (s) are the specific capacitance, the battery working potential and the discharge time of the assembled asymmetric supercapacitor, respectively.

3. Results and discussion

3.1. Structure and morphology characterization

The CuBTC template was obtained through the solvothermal method by copper nitrate and 1,3,5-benzenetricarboxylic acid. Fig. S1a (ESI†) shows the SEM image of CuBTC. It can be seen that solid CuBTC as a precursor is octahedral with a smooth surface and an average side length is approximately 6 μm. In addition, the diffraction peaks of the synthesized CuBTC are consistent with the simulated pattern (Fig. S1b, ESI†) Thermogravimetric analysis (TGA) curves of CuBTC obtained under an oxygen atmosphere are seen in Fig. S2 (ESI†). It is found that CuBTC is weightless at 300 °C, indicating that ligand pyrolysis occurs. When the temperature rises to 500 °C, the mass does not change, indicating that the ligand has been completely pyrolyzed.

Hollow porous CuO and CuO/g-C$_3$N$_4$ were prepared by annealing using CuBTC as a sacrificial template. XRD analysis of the two products was performed as shown in Fig. 1a. It is noticed that the diffraction peaks of the products calcined at 500 °C are all copper oxide peaks (PDF45-0973). At the same time, there are no other impurity peaks, indicating that CuBTC is completely converted to CuO with a hollow structure. After adding g-C$_3$N$_4$, the characteristic peaks of CuO are obviously wider than that before recombination, because of the interaction of two different components, crystalline and amorphous. In addition, the product presents two diffraction peaks at 27.8° and 32.1°, which correspond to the (110) and (200) crystal faces of g-C$_3$N$_4$, respectively, and indicate the successful incorporation of g-C$_3$N$_4$. The SEM analysis of the products obtained shows that the ligand thermolysis of CuBTC results in the formation of CuO with a rough surface and a hollow octahedral structure (Fig. 1b and c). The effects of different calcination
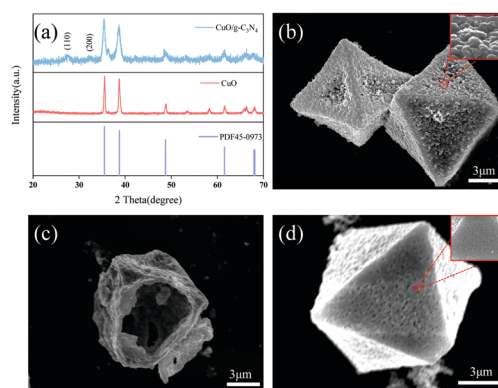

Fig. 1 (a) XRD patterns of CuO/g-C$_3$N$_4$-0.5, (b and c) the SEM images of CuO$_{500}$, and (d) the SEM images of CuO/g-C$_3$N$_4$-0.5.

temperatures on the samples are shown in Fig. S3a–c (ESI†). In the temperature range of 300–500 °C, the higher the temperature extends, the rougher the surface and the more obvious the porous structure becomes. When the temperature reaches 600 °C, the octahedral structure collapses due to the residual stress generated by the transitional pyrolysis of ligands, indicating that calcination temperature has an important influence on the pyrolysis degrees of ligands during the oxidation of CuBTC to CuO. The SEM diagram of the composite prepared at 500 °C shows that the roughness of the porous CuO surface is weakened due to the uniform coating of g-C_3N_4 on the surface (Fig. 1d). At the same time, the g-C_3N_4 coated on the surface of the composite material is relatively stable to maintain the original state under this temperature condition because its thermal decomposition begins above 550 °C.[51] Subsequently, in order to further research the effect of the dosage of g-C_3N_4 on the morphology of the samples, the SEM measurements of CuO/g-C_3N_4 are characterized and the results are shown in Fig. S4 (ESI†). With the increase of g-C_3N_4 content, the agglomeration of the carbon layer on the surface of the product will be more serious. When the mass ratio of CuBTC to g-C_3N_4 is 1:1, it is difficult to observe the octahedral structure.

The structure of the CuO/g-C_3N_4-0.5 composite with a hollow octahedral structure is further detected by TEM, and the typical TEM images are displayed in Fig. 2a. It is clearly seen that the inner side and edge of the sample exhibit significant contrast between light and shade, which well proves the hollow octahedral structure of the CuO/g-C_3N_4-0.5 composite. The average thickness of the shell is 100 nm, which corresponds to the results of SEM. Fig. 2b is a local magnified view of the composite material, indicating that g-C_3N_4 successfully grows on the surface of CuO. Fig. 2c clearly shows the lattice fringe of the CuO/g-C_3N_4 composite material, and the measured lattice spacing is 0.24 nm, pointing to the (111) crystal plane of CuO. Furthermore, Fig. 2d–g are the EDS mapping analysis results of elements corresponding to the CuO/g-C_3N_4 composite. The four elements Cu, O, N and C are uniformly distributed in a single octahedral surface, further demonstrating the successful synthesis of the CuO/g-C_3N_4 composite.

The chemical composition of the samples before and after synthesis was investigated by X-ray photoelectron spectroscopy (XPS). The high-resolution Cu 2p spectra of CuO and CuO/g-C_3N_4 are shown in Fig. 3a. The image is composed of two spin–orbit double peaks and two satellite peaks. The fitting energy bands of characteristic peaks of Cu $2p_{3/2}$ and Cu $2p_{1/2}$ for CuO are 933.6 and 953.7 eV. Furthermore, the satellite peaks at 941.7, 944.1 and 962.1 eV are attributed to three shake-up peaks of Cu at high binding energy sides of Cu $2p_{3/2}$ and Cu $2p_{1/2}$ edges, respectively. It is noteworthy that the binding energy of the Cu $2p_{3/2}$ characteristic peak of CuO/g-C_3N_4 is slightly shifted, indicating a strong interaction between CuO and g-C_3N_4.[52] Fig. 3b shows the O 1s spectra of two samples. The O 1s spectra present two characteristic peaks at the binding energies of 529.9 and 531.8 eV, confirming the presence of the Cu–O bond and C=O bond. The C 1s spectrum and the core level C 1s spectrum of CuO/g-C_3N_4 could be divided into two
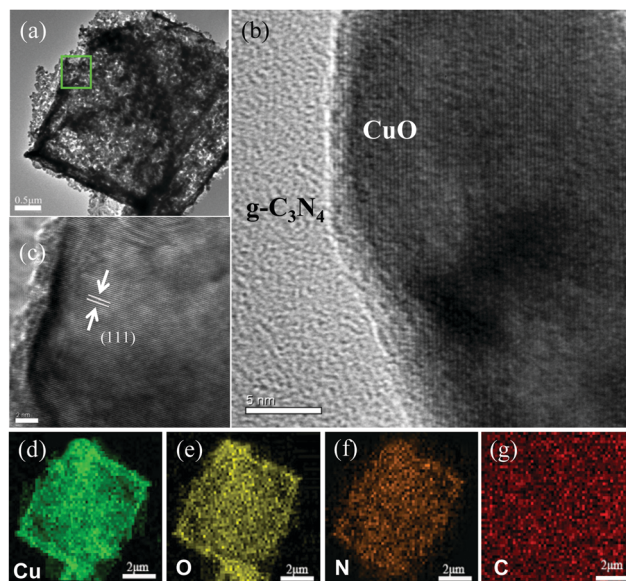

Fig. 2 (a)–(c) HAADF-STEM image of CuO/g-C_3N_4-0.5, and (d)–(g) elemental mapping of CuO/g-C_3N_4-0.5 for Cu, O, N, and C.
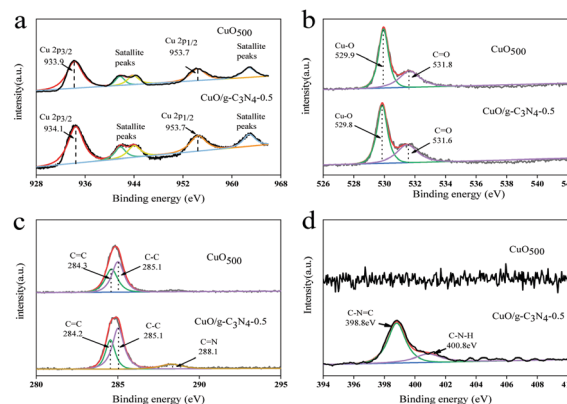

Fig. 3 XPS spectra of three prepared samples: (a) Cu 2p, (b) O 1s, (c) C 1s and (d) N 1s.

bonds. Among them, one peak at 284.6 eV corresponds to the sp² C–C bond originating from the adventitious carbon in species of sample, while the other at 285.1 eV belongs to the C=C bond of the benzene ring in the ligand (Fig. 3c). For CuO/g-C_3N_4, the C=N bond at 288.1 eV may be attributed to g-C_3N_4. The peak strength corresponding to the C–C bond and C=O bond is stronger than before the compound g-C_3N_4, and the peak of C=C is slightly shifted, indicating a high interaction between CuO and g-C_3N_4.[53] Two characteristic peaks at 398.8 and 400.8 eV for CuO/g-C_3N_4 correspond to C–N=C and C–N–H, respectively, while the N 1s spectrum for pure CuO has no obvious characteristic peak (Fig. 3d).

The measurement of specific surface area and mesoporous characteristics of electrode materials is of great significance to evaluate their electrochemical properties. Fig. 4a describes the nitrogen adsorption/desorption isotherms and the corresponding
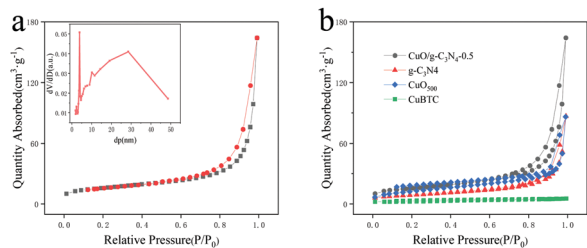
Fig. 4 (a) N_2 adsorption/desorption isotherms and pore size distribution of CuO/g-C_3N_4-0.5; (b) CuBTC, CuO$_{500}$, g-C_3N_4 and CuO/g-C_3N_4-0.5.

Scheme 1 Schematic illustration of the fabrication process of the CuO/g-C_3N_4 composite with a hollow octahedral structure.

Barrett–Joyner–Halenda (BJH, Fig. 4a inset) result of the CuO/g-C_3N_4-0.5 sample. The hollow porous octahedral CuO/g-C_3N_4-0.5 composite with a cladding g-C_3N_4 shell has a specific surface area of up to 61.3211 m^2 g^{-1}. The calculated BET surface area of the CuBTC, CuO$_{500}$ and g-C_3N_4 (Fig. 4b) is only 8.2442, 45.8526 and 30.5337 m^2 g^{-1}, respectively, indicating that the composite of the two different materials can significantly enhance the specific surface area of the material. The larger specific surface area and mesoporous structure can afford more active sites to promote the electron transfer between the electrolyte and the electrode, and also improve the charge storage efficiency. In addition, the adsorption isotherm of the CuO/g-C_3N_4-0.5 composite belongs to the typical IV-H3 hysteresis ring, indicating that the material is a mesoporous material. BJH results show that the composite exhibits a layered hollow structure with the range of pore sizes from 3 nm to 30 nm.[54] These layered pores make the contact area between the active material and the electrolyte large and sufficient, effectively reducing the self-aggregation of the hybrid structure in the course of electrochemical charge–discharge.

The feasible mechanism of CuO/g-C_3N_4 formation as a result of a hollow porous structure is as follows (Scheme 1). First, the CuBTC template with an octahedral structure was synthesized by a facile hydrothermal means. The uniform distribution of Cu^{2+} in the synthesized octahedral precursors provided a metal source for the further formation of CuO. The CuBTC template was then heat-treated in air, resulting in evenly arranged CuO and hollow structures on the surface of CuBTC templates due to heterogeneous shrinkage and ligand pyrolysis during heating treatment. The introduced g-C_3N_4 lamellar structure was heated to the surface of the octahedral structure. The coating uniformity can be effectively regulated through adjusting the amount of g-C_3N_4 and the temperature of heat treatment. The excellent electrochemical performance of composite materials can be attributed to the synergistic effect of CuO and g-C_3N_4, as follows: firstly, the vertical charge transfer path of g-C_3N_4 improves the conductivity of the CuO/g-C_3N_4 composite, which is conducive to rapid electron diffusion during charge and discharge processes. Secondly, the CuO octahedral structure can play a supporting role, prevent excessive aggregation of materials, and facilitate contact with the electrolyte. Finally, due to the hollow structure of the CuO/g-C_3N_4 composite, more active sites are exposed and electrochemical reactions are promoted. In conclusion, the CuO/g-C_3N_4 composite is considered to be an ideal combination of electrodes for supercapacitors.
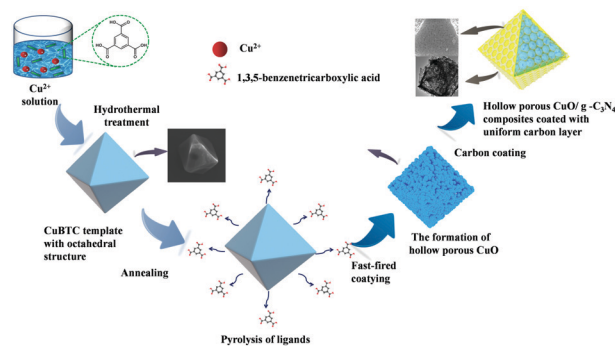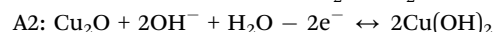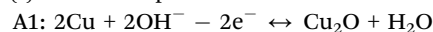
3.2. Electrochemical properties of electrode materials

For investigation of the electrochemical process and kinetic properties, cyclic voltammetry (CV), galvanostatic charge–discharge (GCD) and electrochemical impedance spectroscopy (EIS) measurements were further conducted through a three-electrode system. Fig. S5a (ESI†) shows the GCD curves of CuO at different calcination temperatures at 2 A g^{-1}, showing that the proper calcination temperature can make CuO have a hollow octahedral structure to improve the electrochemical performances. Fig. S5b (ESI†) displays the CV comparison diagram of CuBTC, CuO$_{500}$ and CuO/g-C_3N_4-0.5 at a scanning speed of 10 mV s^{-1}. Both CuO and CuO/g-C_3N_4 have obvious redox peaks, confirming that reversible redox reactions have occurred on the electrode surface, proving that the materials have obvious pseudocapacitance properties. In addition, by calculating the specific capacitance of the integrated area of CV curves, the specific capacitance of the composite material is significantly increased, because the formation of a g-C_3N_4 coated-shell layer is conducive to ion/electron transport and provides more electrochemical active sites. For the detailed description of the effects of g-C_3N_4 dosage on the electrochemical properties, GCD tests were carried out on CuO/g-C_3N_4-0.25, CuO/g-C_3N_4-0.5, CuO/g-C_3N_4-0.75, and CuO/g-C_3N_4-1.0 at 2 A g^{-1} (Fig. S5c, ESI†). The specific capacitance of CuO/g-C_3N_4-0.5 is 1530.4 F g^{-1} at a charge–discharge current density of 2 A g^{-1}, which is more than those of CuO/g-C_3N_4-0.25 (1211.7 F g^{-1}), CuO/g-C_3N_4-0.75 (934.2 F g^{-1}) and CuO/g-C_3N_4-1.0 (769.7 F g^{-1}). This is due to the shell structure of CuO/g-C_3N_4-0.5 products being more uniform and stable than other ratios.

The CV curves of CuO/g-C_3N_4-0.5 at disparate scanning rates are revealed in Fig. 5a. With the increase of scanning speed, the redox peaks lag to both sides, which may be attributed to internal resistance and limitation of the charge transfer. The shape similarity of CV curves indicates remarkable stability of the sample. Anode peaks (A1 and A2) at -0.27 V and 0.19 V correspond to the oxidation of Cu to Cu(I) and Cu(I) to Cu(II), respectively. Similarly, cathode peaks (C1) at -0.90 V are derived from the reduction of Cu(II) to Cu. The possible reactions are as follows:[55,56]
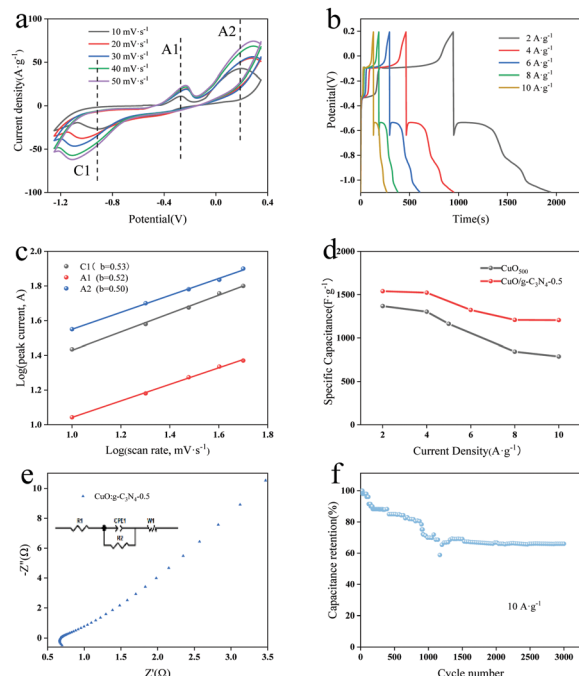
A1: $2Cu + 2OH^- - 2e^- \leftrightarrow Cu_2O + H_2O$

A2: $Cu_2O + 2OH^- + H_2O - 2e^- \leftrightarrow 2Cu(OH)_2$

C1: $Cu + 2OH^- - 2e^- \leftrightarrow Cu(OH)_2$

Fig. 5 (a) CV curves of CuO/g-C$_3$N$_4$-0.5 at scan rates of 10–50 mV s^{-1}; (b) GCD curves of CuO/g-C$_3$N$_4$-0.5 at different current densities; (c) the linear relation between the anodic/cathodic peak currents and the scan rates; (d) specific capacitance *versus* various current densities for CuO/g-C$_3$N$_4$-0.5 and CuO$_{500}$; (e) Nyquist plots of CuO/g-C$_3$N$_4$-0.5, and the inset shows the equivalent circuit; (f) cycling stability performance of CuO/g-C$_3$N$_4$-0.5 at a current density of 10 A g^{-1}.

In general, the capacitance effect is determined by analyzing the volt-ampere response at different scanning speeds. The formula is as follows:

$$i_p = av^b \tag{4}$$

where I_p represents the current density, v represents the scanning surface rate, a and b are constants, b is 1 corresponding to the nondiffusive-controlled surface redox reaction (capacitance effect), and $b = 1/2$ corresponds to the diffusive-controlled surface redox process (battery effect). As shown in Fig. 5c, after linear fitting of peak current and scanning speed, b values corresponding to three peaks are approximately equal to 0.5, which proves to be a typical diffusion control process between the electrode material and electrolyte, and CuO/g-C$_3$N$_4$-0.5 is a representative electrode material.[57] Fig. 5b shows the GCD curve of CuO/g-C$_3$N$_4$-0.5 at 2–10 A g^{-1}. The obvious nonlinear curve further proves the pseudo-capacity characteristic. The specific capacitance calculated based on the charge–discharge curves is shown in Fig. 5d. The specific capacitance is 1530.4 F g^{-1} at 2 A g^{-1}. Even though the current density raises to 10 A g^{-1}, the capacitance retention rate is about 69% (1054.5 F g^{-1}). However, the capacitance retention of CuO$_{500}$ without g-C$_3$N$_4$ is only 57%, which further demonstrates that the introduction of g-C$_3$N$_4$ can strengthen the stability of the composites.

For the sake of further investigation of the electrochemical characterization, electrochemical impedance (EIS) was adopted in the frequency range from 100 k to 0.01 Hz. As known in Fig. 5e, the Nyquist plot of CuO/g-C$_3$N$_4$-0.5 consists of semi-circles in the high frequency region and linear components in the low frequency region. The real axis intercept is the equivalent series resistance (R_s) with a value of 0.68 Ω, which is composed of the ionic resistance of the electrolyte, the inherent resistance of the active material, and the contact resistance between the active material and the collector. The diameter of the semicircle indicates that the internal resistance of charge transfer (R_{ct}) of the system is 1.47 Ω. The smaller the R_{ct} value is, the faster the rate of charge transfer is, because of the formation of the g-C$_3$N$_4$ coated-shell to accelerate the charge transport capacity in the vertical direction. In the low frequency region, the slope of the line is Warburg impedance (Z_W), which is due to the diffusion along the octahedron surface at the electrolytic solution. Low R_s, R_{ct} and Z_W indicate that the hollow porous CuO/g-C$_3$N$_4$ has a larger active specific surface area and higher conductivity, which can extend the electrode reaction zone.[58] It makes the electrode material come into contact with the electrolyte more sufficiently during charge–discharge processes, thus improving its specific capacitance. Furthermore, CuO/g-C$_3$N$_4$ as an anode material has good cycling ability (Fig. 5f). After 3000 cycles the specific capacitance of the CuO/g-C$_3$N$_4$-0.5 electrode material can still retain 66.3% of the initial value at 10 A g^{-1}, which fully proves that the CuO/g-C$_3$N$_4$ electrode material has certain application potential. After the cycling test, the material was analyzed by SEM to explore the material morphology before and after the reaction (Fig. S7, ESI†). After the cycling test, the CuO/g-C$_3$N$_4$ material can still maintain the octahedral structure, and part of g-C$_3$N$_4$ on the surface is off, which may be the reason for the decrease of its specific capacitance.

3.3. Electrochemical performances of ASCs assembled by NiCoMOF//CuO/g-C$_3$N$_4$

The ASC was prepared through NiCoMOF as the positive electrode (Fig. 6a), and its electrochemical properties were investigated by CV and GCD tests in a three-electrode system (Fig. S6a and b, ESI†). In the potential window of 0–0.5 V, the CV curves of NiCoMOF show typical pseudocapacitive characteristics caused by the pseudocapacitive materials. According to the GCD curve, the specific capacitance of NiCoMOF is 828.50 F g^{-1} at 0.5 A g^{-1}. On the base of the charge–discharge balance principle, the mass ratio of positive and negative materials can be determined to be 6.53 : 1. To determine its operating voltage range, Fig. S8 (ESI†) shows the CV diagrams of the NiCoMOF//CuO/g-C$_3$N$_4$ ASC in different voltage ranges (0–1.5 V, 0–1.6 V, 0–1.65 V, 0–1.7 V, and 0–1.8 V). Since there is significant polarization at 0–1.7 V and no polarization at 0–1.6 V, the working voltage is located at 0–1.6 V. Fig. 6b shows the CV curves of the NiCoMOF//CuO/g-C$_3$N$_4$ ASC device in the potential range of 0–1.6 V. At all of the scanning rates, the redox peaks of pseudocapacitance can be obviously observed, demonstrating the excellent stability. Subsequently, the basic
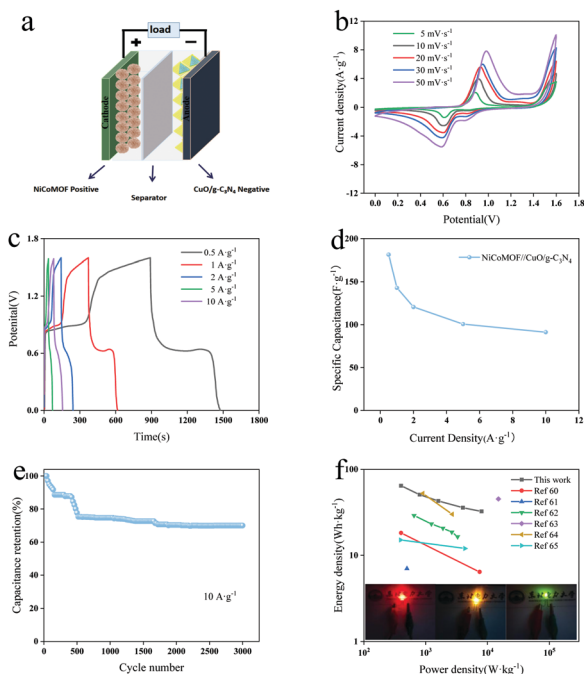
Fig. 6 (a) Schematic illustration of the NiCoMOF//CuO/g-C₃N₄ ASC; (b) CV curves; (c) GCD curves of the NiCoMOF//CuO/g-C₃N₄ ASC at different current densities of 0.5–10 A g^{-1}; (d) specific capacitance *versus* various current densities for the NiCoMOF//CuO/g-C₃N₄ ASC; (e) cycling performance of the NiCoMOF//CuO/g-C₃N₄ ASC at a current density of 10 A g^{-1}; (f) Ragone plot related to the energy and power densities of the NiCoMOF//CuO/g-C₃N₄ ASC and the comparisons with other research studies; the inset shows the photos of the LEDs lit up by the as-fabricated NiCoMOF//CuO/g-C₃N₄ ASC.

symmetry of charge and discharge curves illustrates that ACS devices have good reversibility of charge storage (Fig. 6c). The specific capacitance calculated by the GCD curve is described in Fig. 6d. The specific capacitance of the NiCoMoF//CuO/g-C₃N₄ ASC device is 181.3 F g^{-1} at 0.5 A g^{-1}. The specific capacitance is 91.3 F g^{-1} and the capacitance retention rate is 50.3% even at 10 A g^{-1}. Therefore, the device has good rate performance. And the capacitance can still retain 70.1% of the initial value after 3000 cycles at 5 A g^{-1} (Fig. 6e). The fast capacitance decay in the first 500 cycles is observed in both samples, followed by a very stable state. The relatively rapid capacitance deterioration is probably attributed to the structure collapse, the reduction of active surface area, the phase transformation and an increase of the resistance during charge–discharge processes in alkali environments.[59] The Ragone diagram of the NiCoMOF//CuO/g-C₃N₄ ASC device obtained according to the discharge curve is found in Fig. 6f. As the power density is 800 W kg^{-1}, the energy density of the NiCoMOF//CuO/g-C₃N₄ ASC device is 50.8 W h kg^{-1}, and the device maintains an energy density of 32.4 W h kg^{-1} even at 8000 W kg^{-1}. All these clearly demonstrate the excellent performance of NiCoMOF//CuO/g-C₃N₄ ASC devices. For a better comparison, the electrochemical properties of many other hybrid ultracapacitors are also shown in the Ragone diagram.[60–65] In order to verify its actual electrochemical performance, two prepared NiCoMOF//CuO/g-C₃N₄ ASC

devices were connected in series to power 2.0–2.2 V red, green and yellow LEDs, respectively. The results show that the LEDs can be lit for up to 30 min.

4. Conclusions

In summary, based on the unique precursor CuBTC, two-component CuO/g-C₃N₄ composites were designed through an ultrasonic treatment and rapid thermal annealing. By optimizing the temperature and the content of g-C₃N₄ in thermal annealing reaction, a hollow CuO with a uniform carbon coating displayed high electrochemical performance as an anode material in a three-electrode system and ASC, respectively. This work provides a feasible thought to effectively control the electronic structure and morphology of transition metal compounds with carbon materials to acquire excellent performance and expand a great application on the base of the structural integrity and compositional advantages.

Conflicts of interest

There are no conflicts to declare.

Acknowledgements

Notes and references

1 H. Xie, X. Liu, R. Wu, J. Liu, J. Wu and L. Li, High-Performance Supercapacitor with Faster Energy Storage and Long Cyclic Life Based on CuO@ MnO₂ Nano-Core–Shell Array on Carbon Fiber Surface. *ACS Applied Energy, Materials*, 2020, **3**, 7325–7334.

2 D. P. Dubal, O. Ayyad, V. Ruiz and P. Gomez-Romero, Hybrid energy storage: the merging of battery and supercapacitor chemistries, *Chem. Soc. Rev.*, 2015, **44**, 1777–1790.

3 W. Zuo, C. Xie, P. Xu, Y. Li and J. Liu, A Novel Phase-Transformation Activation Process toward Ni–Mn–O Nanoprism Arrays for 2.4 V Ultrahigh-Voltage Aqueous Supercapacitors, *Adv. Mater.*, 2017, **29**, 1703463.

4 W. Zuo, C. Xie, P. Xu, Y. Li and J. Liu, Battery-supercapacitor hybrid devices: recent progress and future prospects, *Adv. Sci.*, 2017, **4**, 1600539.

5 W. W. Ning, L. B. Chen, W. F. Wei, Y. J. Chen and X. Y. Zhang, NiCoO₂/NiCoP@Ni nanowire arrays: tunable composition and unique structure design for high-performance winding asymmetric hybrid supercapacitors, *Rare Metals*, 2020, **39**, 1034–1044.

6 F. Yu, L. Pang and H. X. Wang, Preparation of mulberry-like RuO₂ electrode material for supercapacitor, *Rare Met.*, 2021, **40**, 440–447.

7   J. Yan, Z. Fan, W. Sun, G. Ning, T. Wei, Q. Zhang and F. Wei, Advanced asymmetric supercapacitors based on $Ni(OH)_2$/graphene and porous graphene electrodes with high energy density, *Adv. Funct. Mater.*, 2012, **22**, 2632–2641.

8   X. Lu, M. Yu, G. Wang, T. Zhai, S. Xie, Y. Ling and Y. Li, H-TiO_2@ MnO_2//H-TiO_2@ C core–shell nanowires for high performance and flexible asymmetric supercapacitors, *Adv. Mater.*, 2013, **25**, 267–272.

9   W. Qiushi, L. Yuhang, M. Tao, H. Binbin, H. Lei, S. Hongjie, M. Changgong and T. Yexiang, Engineering heterostructure-incorporated metal silicates anchored on carbon nanotubes for highly durable lithium storage, *ACS Appl. Energy Mater.*, 2021, **4**, 1548–1559.

10 Q. Wang, T. Meng, Y. Li, J. Yang and Y. Tong, Consecutive chemical bonds reconstructing surface structure of silicon anode for high-performance lithium-ion battery, *Energy Storage Mater.*, 2021, **39**, 354–364.

11 Q. Wang, H. Yang, T. Meng, J. Yang and Y. Tong, Boosting electron transfer with heterointerface effect for high-performance lithium-ion storage, *Energy Storage Mater.*, 2021, **36**, 365–375.

12 Q. Wang, Y. Zhang, H. Jiang, X. Li, Y. Cheng and C. Meng, Designed mesoporous hollow sphere architecture metal (Mn, Co, Ni) silicate: a potential electrode material for flexible all solid-state asymmetric supercapacitor, *Chem. Eng. J.*, 2019, **362**, 818–829.

13 L. Liu, Z. Niu, L. Zhang, W. Zhou, X. Chen and S. Xie, Nanostructured Graphene Composite Papers for Highly Flexible and Foldable Supercapacitors, *Adv. Mater.*, 2014, **26**, 4855–4862.

14 C. Tang, X. Yin and G. Hao, Superior performance asymmetric supercapacitors based on a directly grown commercial mass 3D Co_3O_4@$Ni(OH)_2$ core-shell electrode, *ACS Appl. Mater. Interfaces*, 2013, **5**, 10574–10582.

15 B. Y. Xia, Y. Yan, N. Li, H. B. Wu, X. W. D. Lou and X. Wang, A metal–organic framework-derived bifunctional oxygen electrocatalyst, *Nat. Energy*, 2016, **1**, 15006.

16 Y. Li, K. Ye, K. Cheng, D. Cao, Y. Pan and S. Kong, Anchoring CuO nanoparticles on nitrogen-doped reduced graphene oxide nanosheets as electrode material for supercapacitors, *J. Electroanal. Chem.*, 2014, **727**, 154–162.

17 X. F. Lu, X. Y. Chen, W. Zhou, Y. X. Tong and G. R. Li, α-Fe_2O_3@PANI Core-Shell Nanowire Arrays as Negative Electrodes for Asymmetric Supercapacitors, *ACS Appl. Mater. Interfaces*, 2015, **7**, 14843–14850.

18 J. X. Feng, S. H. Ye, X. F. Lu, Y. X. Tong and G. R. Li, Asymmetric Paper Supercapacitor Based on Amorphous Porous Mn_3O_4 Negative Electrode and $Ni(OH)_2$ Positive Electrode: A Novel and High-Performance Flexible Electrochemical Energy Storage Device, *ACS Appl. Mater. Interfaces*, 2015, **7**, 11444–11451.

19 M. Yu, W. Wang, C. Li, T. Zhai, X. Lu and Y. Tong, Scalable self-growth of Ni@NiO core-shell electrode with ultrahigh capacitance and super-long cyclic stability for supercapacitors, *Npg Asia Mater.*, 2014, **6**, e129.

20 F. Luan, G. Wang, Y. Ling, X. Lu, H. Wang, Y. Tong and Y. Li, High energy density asymmetric supercapacitors with a nickel oxide nanoflake cathode and a 3D reduced graphene oxide anode, *Nanoscale*, 2013, **5**, 7984.

21 X. Jian, H. M. Yang, J. G. Li, E. H. Zhang and Z. H. Liang, Flexible all-solid-state high-performance supercapacitor based on electrochemically synthesized carbon quantum dots/polypyrrole composite electrode, *Electrochim. Acta*, 2017, **228**, 483–493.

22 X. Ma, L. Gan, M. Liu, P. K. Tripathi, Y. Zhao, Z. Xu and L. Chen, Mesoporous size controllable carbon microspheres and their electrochemical performances for supercapacitor electrodes, *J. Mater. Chem. A*, 2014, **2**, 8407–8415.

23 W. Zhe, X. Song, Y. Yang, W. Dong and M. Sun, Recent progress of research of non-enzymatic glucose sensors based on copper, *J. Northeast Electric Power Univ. (Natural Science Edition)*, 2018, **38**, 95–100.

24 J. Cai, H. Niu, Z. Li, Y. Du, P. Cizek, Z. Xie and T. Lin, High-Performance Supercapacitor Electrode Materials from Cellulose-Derived Carbon Nanofibers, *ACS Appl. Mater. Interfaces*, 2015, **7**(27), 14946–14953.

25 Q. Ke and J. Wang, Graphene-based materials for supercapacitor electrodes–A review, *J. Materiomics*, 2016, 37–54.

26 L. Zhang, D. DeArmond, N. T. Alvarez, D. Zhao, T. Wang, G. Hou and V. Shanov, Beyond graphene foam, a new form of three-dimensional graphene for supercapacitor electrodes, *J. Mater. Chem. A*, 2016, **4**, 1876–1886.

27 H. Zhang, X. Tian, C. Wang, H. Luo, J. Hu, Y. Shen and A. Xie, Facile synthesis of RGO/NiO composites and their excellent electromagnetic wave absorption properties, *Appl. Surf. Sci.*, 2014, **314**, 228–232.

28 H. Zhang, X. Tian, C. Wang, H. Luo, J. Hu, Y. Shen and A. Xie, Effect of calcination temperatures on the electrochemical performances of nickel oxide/reduction graphene oxide (NiO/RGO) composites synthesized by hydrothermal method, *J. Phys. Chem. Solids*, 2016, **98**, 209–219.

29 C. Lu, D. Wang, J. Zhao, S. Han and W. Chen, A Continuous Carbon Nitride Polyhedron Assembly for High-Performance Flexible Supercapacitors, *Adv. Funct. Mater.*, 2017, **27**, 1606219.

30 Y. Gong, M. Li and Y. Wang, Carbon Nitride in Energy Conversion and Storage: Recent Advances and Future Prospects, *ChemSusChem*, 2015, **8**, 931–946.

31 L. Xu, J. Xia and X. Hui, *et al.*, Reactable ionic liquid assisted solvothermal synthesis of graphite-like C_3N_4 hybridized α-Fe_2O_3 hollow microspheres with enhanced supercapacitive performance, *J. Power Sources*, 2014, **245**, 866–874.

32 L. Xu, J. Xia, H. Xu, S. Yin, K. Wang, L. Huang and H. Li, Dramatic Activity of C_3N_4/$BiPO_4$ Photocatalyst with Core/Shell Structure Formed by Self-Assembly, *Adv. Funct. Mater.*, 2012, **22**, 1518–1524.

33 J. Wang and W. D. Zhang, Modification of TiO_2 nanorod arrays by graphite-like C_3N_4 with high visible light photoelectrochemical activity, *Electrochim. Acta*, 2012, **71**, 10–16.

34 P. Shi, L. Li, L. Hua, Q. Qian, P. Wang, J. Zhou and W. Huang, Design of Amorphous Manganese Oxide@Multi-Walled Carbon Nanotube Fiber for Robust Solid-State Supercapacitor, *ACS Nano*, 2017, **11**, 444–452.

35 E. C. Cho, C. W. Chang-Jian, K. C. Lee, J. H. Huang, B. C. Ho, R. Z. Liu and Y. S. Hsiao, Ternary composite based on homogeneous Ni(OH)$_2$ on graphene with Ag nanoparticles as nanospacers for efficient supercapacitor, *Chem. Eng. J.*, 2018, **334**, 2058–2067.

36 G. Qu, J. Cheng, X. Li, D. Yuan, P. Chen, X. Chen and H. Peng, A Fiber Supercapacitor with High Energy Density Based on Hollow Graphene/Conducting Polymer Fiber Electrode, *Adv. Mater.*, 2016, **28**, 3646–3652.

37 T. Liu, C. Jiang, W. You and J. Yu, Hierarchical porous C/MnO$_2$ composite hollow microspheres with enhanced supercapacitor performance, *J. Mater. Chem. A*, 2017, **5**, 8635–8643.

38 B. Li, Q. Sun, R. Yang, D. Li and Z. Li, Simple preparation of graphene-decorated NiCo$_2$O$_4$ hollow nanospheres with enhanced performance for supercapacitor, *J. Mater. Sci.: Mater. Electron.*, 2018, **29**, 7681–7691.

39 W. Lu, M. Liu, L. Miao, D. Zhu, X. Wang, H. Duan and L. Chen, Nitrogen-containing ultramicroporous carbon nanospheres for high performance supercapacitor electrodes, *Electrochim. Acta*, 2016, **205**, 132–141.

40 K. Shen, F. Ran, X. Zhang, C. Liu, N. Wang, X. Niu and S. Chen, Supercapacitor electrodes based on nano-polyaniline deposited on hollow carbon spheres derived from cross-linked co-polymers, *Synth. Met.*, 2015, **209**, 369–376.

41 Z. Li, L. Zhang, B. Li, Z. Liu, Z. Liu, H. Wang and Q. Li, Convenient and large-scale synthesis of hollow graphene-like nanocages for electrochemical supercapacitor application, *Chem. Eng. J.*, 2017, **313**, 1242–1250.

42 Z. Li, X. Jiao, C. Li and D. Chen, Synthesis and application of nanocages in supercapacitors, *Chem. Eng. J.*, 2018, **351**, 135–156.

43 Z. Li, L. Zhang, X. Chen, B. Li, H. Wang and Q. Li, Three-dimensional graphene-like porous carbon nanosheets derived from molecular precursor for high-performance supercapacitor application, *Electrochim. Acta*, 2019, **296**, 8–17.

44 R. R. Salunkhe, Y. V. Kaneti and Y. Yamauchi, Metal-Organic Framework-Derived Nanoporous Metal Oxides toward Supercapacitor Applications: Progress and Prospects, *ACS Nano*, 2017, **11**, 5293–5308.

45 L. Wang, Y. Han, X. Feng, J. Zhou, P. Qi and B. Wang, Metal-organic frameworks for energy storage: batteries and supercapacitors, *Coord. Chem. Rev.*, 2016, **307**, 361–381.

46 S. Hou, X. Xu, M. Wang, Y. Xu, T. Lu, Y. Yao and L. Pan, Carbon-incorporated Janus-type Ni$_2$P/Ni hollow spheres for high performance hybrid supercapacitors, *J. Mater. Chem. A*, 2017, **5**, 19054–19061.

47 B. Y. Guan, A. Kushima, L. Yu, S. Li, J. Li and X. W. Lou, Coordination Polymers Derived General Synthesis of Multi-shelled Mixed Metal-Oxide Particles for Hybrid Supercapacitors, *Adv. Mater.*, 2017, **29**, 1605902.

48 X. Xu, J. Liu, J. Liu, L. Ouyang, R. Hu, H. Wang and M. Zhu, A general metal–organic framework (mof)-derived selenidation strategy for in situ carbon-encapsulated metal

49 M. Wei, J. Yang, C. Zheng, P. Xiong and Y. Li, Zn-doped Ni-MOF material with a high supercapacitive performance, *J. Mater. Chem. A*, 2014, **2**, 19005.

50 S. G. Mohamed, I. Hussain and J. J. Shim, One-step synthesis of hollow C-NiCo$_2$S$_4$ nanostructures for high-performance supercapacitor electrodes, *Nanoscale*, 2018, **10**, 6620–6628.

51 Z. S. Hang, L. H. Tan, Y. A. Huang, S. J. Ying and F. M. Xu, Non-isothermal kinetics studies on the thermal decomposition of g-C$_3$N$_4$ by TG Method, *J. Funct. Mater.*, 2011, **42**, 329–332.

52 X. Liu, G. Liu, L. Wang, Y. Li, Y. Ma and J. Ma, Morphology- and facet-controlled synthesis of CuO micro/nanomaterials and analysis of their lithium ion storage properties, *J. Power Sources*, 2016, **312**, 199–206.

53 Y. Shao, M. F. El-Kady, C. W. Lin, G. Zhu, K. L. Marsh, J. Y. Hwang and R. B. Kaner, 3D Freeze-Casting of Cellular Graphene Films for Ultrahigh-Power-Density Supercapacitors, *Adv. Mater.*, 2016, **28**, 6719–6726.

54 M. Thommes, K. Kaneko, A. V. Neimark, J. P. Olivier, F. Rodriguez-Reinoso, J. Rouquerol and K. S. Sing, Physisorption of gases, with special reference to the evaluation of surface area and pore size distribution (IUPAC Technical Report), *Pure Appl. Chem.*, 2015, **87**, 1051–1069.

55 D. O. Miles, D. Jiang, A. D. Burrows, J. E. Halls and F. Marken, Conformal transformation of [Co(BDC)(DMF)] (Co-MOF-71, BDC = 1,4-benzenedicarboxylate, DMF = *N,N*-dimethylformamide) into porous electrochemically active cobalt hydroxide, *Electrochem. Commun.*, 2013, **27**, 9–13.

56 A. Vk, B. Sr, C. Hmy, C. Akk, D. SS and C. SS, Facile synthesis of CuO/NiO/nitrogen doped rGO by ultrasonication for high performance supercapacitors, *J. Alloys Compd.*, 2020, **847**, 156411.

57 Q. Wang, F. Gao, B. Xu, F. Cai, F. Zhan, F. Gao and Q. Wang, ZIF-67 derived amorphous CoNi$_2$S$_4$ nanocages with nanosheet arrays on the shell for a high-performance asymmetric supercapacitor, *Chem. Eng. J.*, 2017, **327**, 387–396.

58 D. Du, R. Lan, W. Xu, R. Beanland, H. Wang and S. Tao, Preparation of a hybrid Cu$_2$O/CuMoO$_4$ nanosheet electrode for high-performance asymmetric supercapacitors, *J. Mater. Chem. A*, 2016, **4**, 17749–17756.

59 J. Xu, S. Gai, F. He, N. Niu, P. Gao and Y. Chen, A sandwich-type three-dimensional layered double hydroxide nanosheet array/graphene composite: fabrication and high supercapacitor performance, *J. Mater. Chem. A*, 2013, **2**, 1022–1031.

60 H. Guan, P. Cai, X. Zhang, Y. Zhang, G. Chen and C. Dong, Cu$_2$O templating strategy for the synthesis of octahedral Cu$_2$O@Mn(OH)$_2$ core–shell hierarchical structures with a superior performance supercapacitor, *J. Mater. Chem. A*, 2018, **6**, 13668–13675.

61 B. Vidhyadharan, I. I. Misnon, R. Abd Aziz, K. P. Padmasree, M. M. Yusoff and R. Jose, Superior supercapacitive performance in electrospun copper oxide nanowire electrodes, *J. Mater. Chem. A*, 2014, **2**, 6578–6588.

62 X. Xu, Y. Liu, P. Dong, P. M. Ajayan, J. Shen and M. Ye, Mesostructured CuCo$_2$S$_4$/CuCo$_2$O$_4$ nanoflowers as advanced electrodes for asymmetric supercapacitors, *J. Power Sources*, 2018, **400**, 96–103.

63 A. A. Ensafi, S. E. Moosavifard, B. Rezaei and S. K. Kaverlavani, Engineering onion-like nanoporous $CuCo_2O_4$ hollow spheres derived from bimetal–organic frameworks for high-performance asymmetric supercapacitors, *J. Mater. Chem. A*, 2018, **6**, 10497–10506.

64 X. He, X. Mao, C. Zhang, W. Yang, Y. Zhou, Y. Yang and J. Xu, Flexible binder-free hierarchical copper sulfide/carbon cloth hybrid supercapacitor electrodes and the application as negative electrodes in asymmetric supercapacitor, *J. Mater. Sci.: Mater. Electron.*, 2020, **31**, 2145–2152.

65 X. He, X. Mao, C. Zhang, W. Yang, Y. Zhou, Y. Yang and J. Xu, Solvothermal Synthesis of 3D Hierarchical CuS Microspheres from a Cu-based Ionic Liquid Precursor for High-Performance Asymmetric Supercapacitors, *ACS Appl. Mater. Interfaces*, 2015, **7**, 21735–21744.